



High- Q , low-index-contrast photonic crystal nanofiber cavity for high sensitivity refractive index sensing

DAQUAN YANG,^{1,3}  XIN CHEN,¹ XUAN ZHANG,¹ CHUWEN LAN,¹ AND YING ZHANG^{2,*}

¹State Key Laboratory of Information Photonics and Optical Communications, School of Information and Communication Engineering, Beijing University of Posts and Telecommunications, Beijing 100876, China

²School of Life Science, Beijing Institute of Technology, Beijing 100081, China

³e-mail: yangdq5896@163.com

*Corresponding author: zhangying3409@bit.edu.cn

Received 21 June 2018; revised 20 July 2018; accepted 20 July 2018; posted 20 July 2018 (Doc. ID 335801); published 15 August 2018

We present the design of simultaneous high-quality (Q)-factor and high-sensitivity (S) photonic crystal nanofiber cavities (PCNFCs) made of single silica nanofiber that have a low-index contrast (ratio = 1.45). By using the three-dimensional finite-difference time-domain method, two different resonant modes, dielectric mode (DM) and air mode (AM), are designed and optimized to achieve an ultrahigh figure of merit (FOM), respectively. Numerical simulations are performed to study the Q -factors and sensitivities of the proposed PCNFCs. It shows that for both DM- and AM-based PCNFCs, respectively, the Q -factors and sensitivities of $Q \sim 1.1 \times 10^7$, $S = 563.6 \text{ nm}/\text{RIU}$ and $Q \sim 2.1 \times 10^5$, $S = 736.8 \text{ nm}/\text{RIU}$ can be estimated, resulting in FOMs as high as 4.31×10^6 and 1.13×10^5 , respectively. To the best of our knowledge, this is the first silica nanofiber cavity geometry that simultaneously features high Q and high S for both DM and AM in PCNFCs. Compared with the state of the art of nanofiber-based cavities, the cavity Q -factor to mode volume (V) ratio (Q/V) in this work has been improved more than two orders of magnitude. The demonstration of a high Q/V cavity in low-index-contrast nanofibers can open up versatile applications using a broad range of functional and flexible fibers. Moreover, due to the extended evanescent field and small mode volumes, the proposed PCNFCs are ideal platforms for remote ultra-sensitive refractive-index-based gas sensing without the need for complicated coupling systems. © 2018 Optical Society of America

OCIS codes: (060.2370) Fiber optics sensors; (230.5298) Photonic crystals; (140.3948) Microcavity devices; (060.2280) Fiber design and fabrication; (280.4788) Optical sensing and sensors.

<https://doi.org/10.1364/AO.57.006958>

1. INTRODUCTION

On-chip integrated optical microcavity sensors, which can significantly enhance light-matter interaction, are renowned for performing ultra-sensitive nanoparticle detection and label-free biosensing [1]. Among all of the on-chip optical microcavity sensor geometries, the silicon-on-insulator (SOI)-based photonic crystal (PC) cavity sensors are advantageous for their high quality (Q)-factor to mode volume (V) ratio (Q/V) [2,3]. Particularly, compared with two-dimensional (2D) PC slab cavity sensors, one-dimensional (1D) PC nanobeam cavity sensors [4–19] with a high figure of merit (FOM) have recently attracted considerable interest for sensing applications due to their attractive properties of ultra-compact footprint, ultrahigh Q/V , and convenient integration with bus-waveguides [20]. Furthermore, recent progress on fabrication technologies for CMOS compatible processes has enabled us to fabricate PC devices using photolithography [21], which will accelerate their

industrialization. However, although the coupling between a PC nanocavity and waveguides can be well designed, the coupling efficiency between an optical fiber and a silicon PC cavity/waveguide is usually not high due to the mode mismatch between the waveguide and the optical fiber.

To overcome this problem, SU-8 bus-waveguides and tapered nanofibers (NFs) have been used to couple the light into the PC devices [7,22]. Particularly, for silicon PC waveguides, tapered NF can couple the light evanescently into the PC devices and achieve very high coupling efficiency, as high as 95% [23]. For the above-mentioned tapered NF coupling systems, the coupling efficiency is very sensitive to the gap between the tapered NF and the PC waveguide. To precisely control the gap size, a xyz translation stage and an objective lens imaging system are necessary. In addition, to achieve efficient coupling, a complicated calibration system is also required, resulting in the devices having fragile packaging and alignment and expensive

cost. However, from the practical application perspective, when designing a portable device, with limited space for off-chip optical components, one needs to make the packaging and alignment robust and cost effective.

Towards this direction, in recent years, the optical NF-based microcavities [24–27] have been demonstrated as prominent candidates for sensing applications and have been widely used in sensor design [28–37], due to their advantageous properties of strong light confinement, ultrahigh transmission, enhanced evanescent fields, and also simultaneously performing as a sensor and a waveguide without the need for complicated coupling systems. So far, most optical NF-based microcavities belong to the Fabry–Perot (FP) cavity type, in which the design of mirrors for FP cavities commonly include interfaces of fiber ends and defects [38,39] and fiber Bragg gratings [40,41]. However, although the optical NF-based microcavities mentioned above have shown extraordinary performance in some specific fields, they also have some shortcomings. For example, the NF-based microcavity sensors with interfaces as mirrors composed of two independent optical fibers need to be carefully aligned, which is not convenient or stable in the application of environmental monitoring. On the other hand, the length of a traditional fiber Bragg grating usually consists of hundreds of periods, indicating a large mode volume, and thus severely decreases the interactions between light and the surrounding medium in close proximity to the NF surface. In particular, it has been a challenge to achieve simultaneously high- Q -factor and small-mode-volume PC cavities made of silica NF due to the low-index contrast ($n_{\text{silicon}}/n_{\text{air}} \sim 1.45$).

To tackle these problems mentioned above, in this paper we propose and theoretically investigate a novel ultra-compact 1D PC NF cavity (PCNFC) for simultaneous high- Q and high-sensitivity refractive index (RI) sensing. By designing a high- Q 1D PC nanocavity in a NF with a low-index contrast (ratio = 1.45), the cavity-enhanced extremely concentrated field with small mode volume causes strong interactions between light and analytes for highly sensitive optical sensing. By using the 3D-finite-difference time-domain (3D-FDTD) method, two different resonant modes, dielectric mode (DM) and air mode (AM), are designed and optimized to achieve ultrahigh FOM, respectively. Here, the sensor FOM is defined as $\text{FOM} = S \cdot Q/\lambda_{\text{res}}$, where, λ_{res} is the resonance wavelength of the PCNFC, and S and Q are the RI sensitivity and quality factor of the PCNFC, respectively. In simulation, as an optical gas sensor, both proposed DM- and AM-based PCNFC designs achieved ultrahigh FOM. For the DM-based PCNFC sensor design, a high Q of 1.1×10^7 and a high sensitivity of 563.6 nm/RIU (RIU = RI unit) can be simultaneously achieved, and a sensor FOM as high as 4.31×10^6 . For the AM-based PCNFC sensor design, a high Q of 2.1×10^5 and a high sensitivity of 736.8 nm/RIU can be simultaneously achieved, and a sensor FOM as high as 1.13×10^5 . This is, to the best of our knowledge, the first PCNFC structure that has simultaneously ultrahigh Q and S for both DM and AM. Moreover, by integrating a 1D PC nanocavity into a freely suspended optical NF, the proposed PCNFC offers a convenient and stable method for long-distance gas sensing without the need for complicated coupling systems and is free from the influence of substrates.

The organization of this paper is as follows. In Section 2, two different PCNFCs, DM-PCNFC and AM-PCNFC, are proposed and theoretically investigated. Both the DM-PCNFC and the AM-PCNFC cavity designs are described in detail. Moreover, the dependence of cavity resonance frequency and Q/V on the number of air-hole gratings N_t and N_m of the proposed DM-PCNFC and AM-PCNFC is investigated, respectively, when the cavity's other geometrical parameters are kept fixed. The numerical simulations are used to analyze and confirm that both the DM-PCNFC and AM-PCNFC platforms are suitable for ultra-sensitive nanosensors. In Section 3, based on 3D-FDTD calculated transmission spectra and field distributions, the feasibility and performance of the PCNFC sensor are analyzed and confirmed. In order to illustrate the working of the proposed sensor device, we fill the sensing area with analytes possessing different RIs. The sensitivity is determined by observing the shifts in the resonant wavelength ($\Delta\lambda$) of the resonators as a function of the variations in RI (ΔRI) in the region surrounding the sensors. Finally, in Section 4, we draw a brief conclusion.

2. HIGH- Q , LOW-INDEX-CONTRAST PCNFC DESIGN

A. Dielectric-Mode-Based PCNFC

The proposed DM-PCNFC geometry consists of a single silica NF waveguide perforated with gratings of circle holes, as shown in Fig. 1(a). In our design, a silica NF waveguide is suspended in free space with circular air holes drilled along the x direction periodically, in which x is the in-plane coordinate along the long axis of the NF. The diameter of the NF is $d_{\text{NF}} = 1.04 \mu\text{m}$. Here, we considered a NF cavity having RI $n_{\text{silicon}} = 1.45$ surrounded by air background with RI $n_{\text{air}} = 1.0$, which is suitable for gas-sensing applications. The cavity was designed using the deterministic high- Q design method that we previously introduced [6,10,42]. As shown in Fig. 1(a), the distances between neighboring holes, namely, the periodicity (a), are kept the same as $a = 620 \text{ nm}$ to form a PC lattice. The structure is symmetric with respect to the center (the red dashed line). A basic DM-PCNFC cavity is formed by parabolically changing radii of the hole gratings while keeping the periodicity and NF diameter unchanged. To achieve high- Q , (1) the radii of air-hole gratings in the taper region are parabolically decreased from $r_{\text{center}} = 0.37a = 230 \text{ nm}$ in the center to $r_{\text{end}} = 0.29a = 180 \text{ nm}$ on both sides, i.e., $r_i = r_{\text{center}} + (i-1)^2(r_{\text{end}} - r_{\text{center}})/(N_t - 1)^2$, where i increases from 1 to N_t , and N_t represents the air-hole gratings number in the taper region. The design of the parabolically tapered hole structure is based on mode matching, which produces a significantly enhanced Q -factor and optical transmission through reductions in propagation losses and scattering that occur locally at transitions between the taper region and the mirror region of the cavity. (2) The radii of air-hole gratings in the mirror region are kept fixed as $r_j = r_{\text{end}} = 180 \text{ nm}$, where j increases from 1 to N_m , and N_m represents the air-hole gratings number in the mirror region. Here, the radii of air-hole gratings in the mirror region kept fixed as $r_{\text{end}} = 180 \text{ nm}$ are chosen from the numerical band diagram simulations, as it gives maximum mirror strength, as shown in Figs. 2(a) and 2(b), respectively.

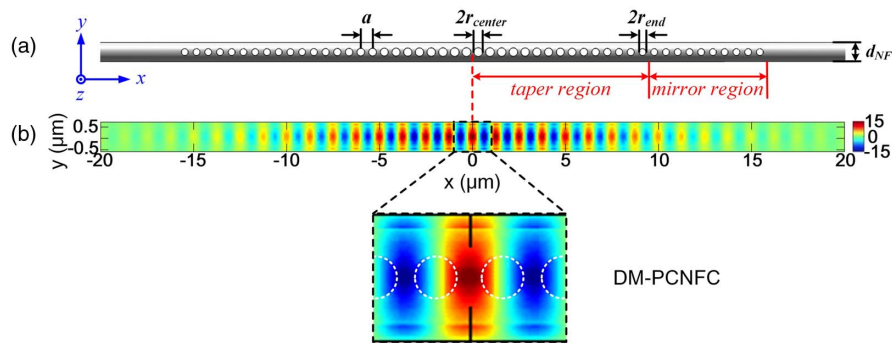


Fig. 1. (a) Schematic illustrations of the proposed dielectric-mode photonic crystal nanofiber cavity (DM-PCNFC). The structure is symmetric with respect to its center (red dashed line). (b) Calculated E_y distribution (top view with $z = 0$) of the fundamental dielectric mode in cavity, where $a = 620$ nm, $d_{\text{NF}} = 1.04$ μm , $r_{\text{center}} = 230$ nm, $r_{\text{end}} = 180$ nm, $N_t = 15$, and $N_m = 10$ are chosen. The white dashed circles indicate the air-hole structure. The unit of the x/y axes is micrometers (μm).

Figure 2(a) shows the transverse electric (TE) band diagrams of the single silica PCNFC with $r = 230$ nm and $r = 180$ nm, respectively. Here, in order to display the photonic bandgaps (PBGs) in the TE band diagram clearly, we draw only the first bands above and below the PBGs (namely, the AM and DM for each air-hole radius [11]), which are below the light line. And the other band curves above the light line for each air-hole radius are not displayed in the TE band diagram [Fig. 2(a)]. The 3D-FDTD method (Lumerical Solutions Inc. [43]) with Bloch boundary conditions was utilized for the simulations. As expected, when the air-hole radius decreases, resulting in the effective RI increasing, the PBG of the structure moves to lower frequency. So the PBG for the structure with $r_{\text{center}} = 230$ nm (red line with dots) is higher than the one for $r_{\text{end}} = 180$ nm (blue line with small triangles). Here, the green dot in the inset of Fig. 2(a) indicates the target DM resonance frequency (at 211.1 THz) of the reported single DM-PCNFC cavity. Figure 2(b) shows the calculated mirror strength γ , for different air-hole radii, can be calculated using $\sqrt{(\omega_2 - \omega_1)^2 / (\omega_2 + \omega_1)^2 - (\omega_{\text{res}} - \omega_0)^2 / \omega_0^2}$, where ω_{res} is the DM-PCNFC target resonant frequency; and ω_2 , ω_1 , and ω_0 are the air band edge, dielectric band edge, and

mid-gap frequency of each segment, respectively. As seen in Fig. 2(b), when the air-hole radius $r = 180$ nm, the maximum mirror strength is obtained. Thus, the radius of the air-hole grating in the mirror region kept fixed as $r_{\text{end}} = 180$ nm is chosen to build DM-PCNFC design.

In order to obtain a DM with high Q/V , the dependence of Q -factor and mode volume on the number of air-hole gratings N_t and N_m of the proposed DM-PCNFC is investigated, respectively, when the cavity's other geometrical parameters are kept fixed as $d_{\text{NF}} = 1.04$ μm , $a = 620$ nm, $r_{\text{center}} = 230$ nm, and $r_{\text{end}} = 180$ nm. First, as shown in Fig. 3(a), we investigate the influence of period gratings number N_t (changed from $N_t = 20$ to $N_t = 80$) on the cavity resonance frequency and Q/V , and there is no additional mirror region outside the taper region, namely $N_m = 0$. As seen, with the period gratings number N_t increasing, the cavity resonance frequency moves slightly towards higher frequency, and the cavity Q/V increases exponentially. When N_t is large enough, the ultrahigh $Q/V > 2.45 \times 10^6$ and the largest Q -factor as high as 1.1×10^7 of the DM can be achieved. However, from the practical application perspective, if the period gratings number N_t is too large, the cavity mechanical feature is fragile, and the

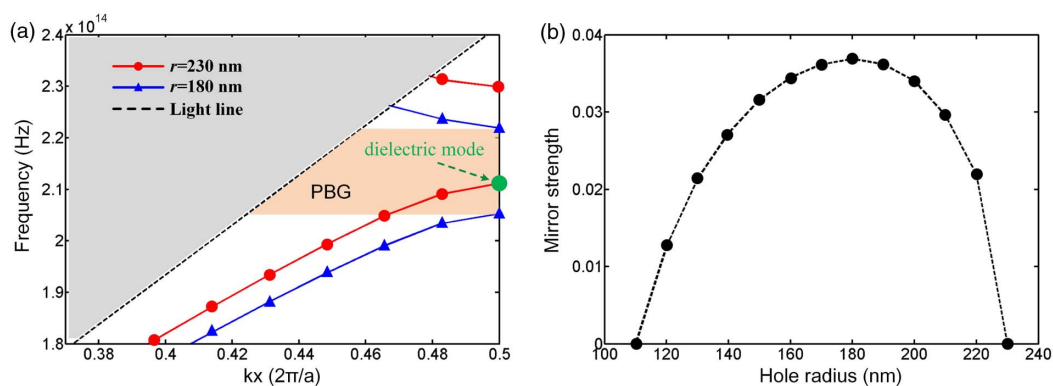


Fig. 2. (a) TE band diagrams for the DM-PCNFC with air-hole radius $r = 230$ nm (red line with dots) and $r = 180$ nm (blue line with small triangles), respectively. In both cases, the nanofiber diameter and periodicity are maintained at $d_{\text{NF}} = 1.04$ μm and $a = 620$ nm, respectively. The green dot indicates the target resonance frequency (at 211.1 THz) of the dielectric mode in PCNFC. (b) Mirror strengths obtained using 3D band diagram simulation for different hole radii, while other structure parameters are kept the same as in (a).

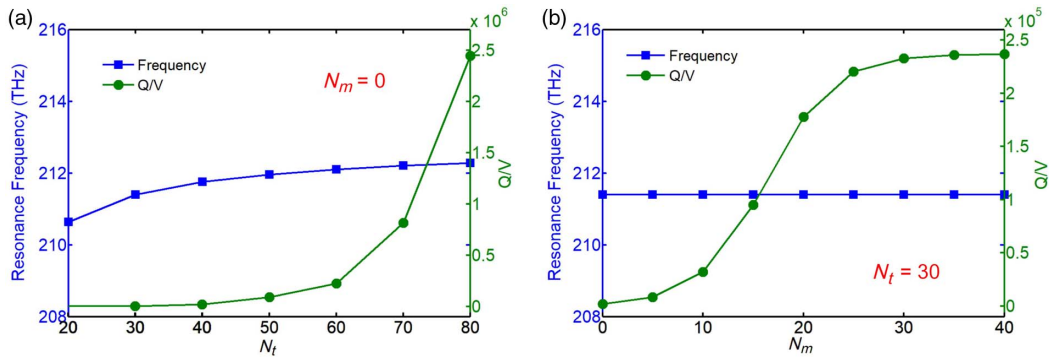


Fig. 3. (a) Influence of different hole grating number N_t (changed from $N_t = 20$ to $N_t = 80$) in the taper region of the proposed DM-PCNFC on cavity resonance frequency and Q/V , when $N_m = 0$. (b) Influence of different hole grating number N_m (changed from $N_m = 0$ to $N_m = 40$) in the mirror region of the proposed DM-PCNFC on cavity resonance frequency and Q/V , when $N_t = 30$. Other parameters are the same as $d_{NF} = 1.04 \mu\text{m}$, $a = 620 \text{ nm}$, $r_{\text{center}} = 230 \text{ nm}$, and $r_{\text{end}} = 180 \text{ nm}$.

cavity fabrication is very challenging. In addition, the large number of period gratings in the taper region will result in large mode volume, which is not conducive to achieving high-sensitivity RI sensing.

Thus, to overcome the limitations above and achieve a radiation- Q -limited cavity, we place additional mirror segments at both ends of the taper regions to improve the cavity Q and V . As shown in Fig. 3(b), we investigate the influence of period gratings number N_m (changed from $N_m = 0$ to $N_m = 40$) in the mirror region on the cavity resonance frequency and Q/V , and the number of the period grating in the taper region is kept fixed as $N_t = 30$. As seen, with the period gratings number N_m increasing, the cavity resonance frequency is nearly invariant under different N_m , and the cavity Q/V first increases exponentially with increasing N_m owing to the mirror's strengthened optical confinement and effectively reduced scattering losses by the increased mirror periods, until it finally levels off when N_m is greater than 25. The high $Q/V \sim 2.37 \times 10^5$ can be achieved. Compared to the cavity without mirror periods (i.e., $N_t = 30$, $N_m = 0$), the cavity Q/V is improved more than two orders of magnitude. The optimized Q -factor is as high as 6.95×10^5 , which is more than two orders of magnitude higher than recent work (simulated $Q \sim 4000$) [33].

Moreover, the cavity mode volume as small as $2.93(\lambda/n_{\text{SiO}_2})^3$ is obtained, and the resonant frequency is 211.4 THz, which agrees very well with the target resonant wavelength obtained at 211.1 THz from the band-diagram simulations, marked as green dots in the inset of Fig. 2(a). Figure 1(b) shows the top view of the major field distribution profile (E_y) in x - y plane of the proposed DM-PCNFC. It can be seen clearly that the majority of the electric field is strongly localized in the center of DM-PCNFC, indicating that a strong interaction between the analytes and the cavity mode can be achieved. Thus, the proposed DM-PCNFC in this paper is potentially an ideal platform for high-sensitive RI-based gas sensing.

B. Air-Mode-Based PCNFC

Figure 4(a) shows the proposed AM-PCNFC geometry consisting of a single silica nanofiber waveguide perforated with gratings of circle holes. Here, the proposed AM-PCNFC cavity is also designed using the same deterministic high- Q design method that we introduced in the above section. As shown in Fig. 4(a), the periodicity and NF diameter are kept fixed as $a = 620 \text{ nm}$, $d_{NF} = 1.04 \mu\text{m}$. To achieve high Q -factor, (1) the radii of air-hole gratings in the taper region are parabolically increased from $r_{\text{center}} = 195 \text{ nm}$ in the center to

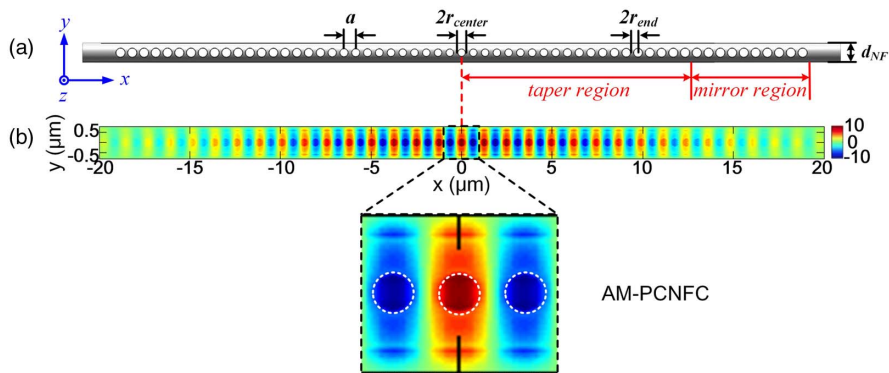


Fig. 4. (a) Schematic illustrations of the proposed air-mode photonic crystal nanofiber cavity (AM-PCNFC). The structure is symmetric with respect to its center (red dashed line). (b) Calculated E_y distribution (top view with $z = 0$) of the fundamental dielectric mode in cavity, where $a = 620 \text{ nm}$, $d_{NF} = 1.04 \mu\text{m}$, $r_{\text{center}} = 195 \text{ nm}$, $r_{\text{end}} = 240 \text{ nm}$, $N_t = 20$, and $N_m = 10$ are chosen. The white dashed circles indicate the air-hole structure. The unit of the x/y axes is micrometers (μm).

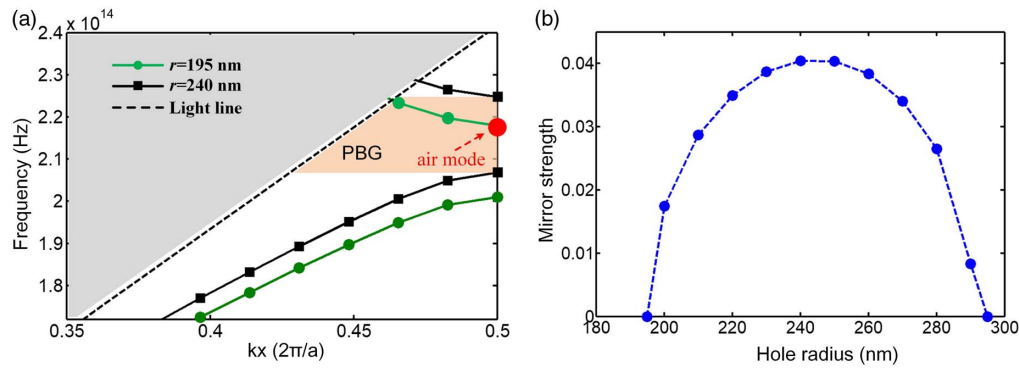


Fig. 5. (a) TE band diagram for the AM-PCNFC with air-hole radius $r = 195$ nm (green line with circle) and $r = 240$ nm (black line with square). In both cases, the nanofiber diameter and periodicity are maintained at $d_{\text{NF}} = 1.04$ μm and $a = 620$ nm, respectively. The red dot indicates the target resonance frequency (at 218.3 THz) of the air mode in PCNFC. (b) Mirror strengths obtained using 3D band diagram simulation for different hole radii, while other structure parameters are kept the same as in (a).

$r_{\text{end}} = 240$ nm on both sides, i.e., $r_i = r_{\text{center}} + (i - 1)^2 (r_{\text{end}} - r_{\text{center}}) / (N_t - 1)^2$, where i increases from 1 to N_t , and N_t represents the air-hole gratings number in the taper region. (2) The radii of air-hole gratings in the mirror region are kept fixed as $r_j = r_{\text{end}} = 240$ nm, where j increases from 1 to N_m , and N_m represents the air-hole gratings number in the mirror region. Here, the radius of air-hole gratings in the mirror region kept fixed as $r_{\text{end}} = 240$ nm is chosen from the numerical band-diagram simulations, as it gives maximum mirror strength, as shown in Figs. 5(a) and 5(b), respectively. Figure 5(a) shows the TE band diagrams of the silica AM-PCNFC with air-hole radius $r = 195$ nm (green line with circle) and $r = 240$ nm (black line with square). Here, the red dot in the inset of Fig. 5(a) indicates the target resonance frequency of AM (at 218.3 THz) in the reported AM-PCNFC cavity. Figure 5(b) shows the calculated mirror strength γ , for different air-hole radii. As seen, when the air-hole radius $r = 240$ nm, the maximum mirror strength is obtained. Thus, the radius of the air-hole grating in the mirror region kept fixed as $r_{\text{end}} = 240$ nm is chosen to build AM-PCNFC design.

In order to obtain an AM with high Q/V , the dependence of Q -factor and mode volume on the number of air-hole gratings N_t and N_m of the proposed AM-PCNFC is also

investigated, respectively, when the cavity's other geometrical parameters are kept fixed as $d_{\text{NF}} = 1.04$ μm , $a = 620$ nm, $r_{\text{center}} = 195$ nm, and $r_{\text{end}} = 240$ nm. Figure 6(a) shows the influence of period gratings number N_t (changed from $N_t = 20$ to $N_t = 80$) on the cavity resonance frequency and Q/V when there is no additional mirror region outside the taper region, namely, $N_m = 0$. As seen, with the period gratings number N_t increasing, the cavity resonance frequency moves slightly towards lower frequency, and the cavity Q/V significantly increases. When N_t is large enough, the ultrahigh $Q/V > 1.42 \times 10^4$ and the largest Q -factor as high as 2.1×10^5 of the AM can be achieved. Figure 6(b) shows the influence of period gratings number N_m (changed from $N_m = 0$ to $N_m = 40$) on the cavity resonance frequency and Q/V when the number of the period grating in the taper region is kept fixed as $N_t = 20$. As seen, with the period gratings number N_m increasing, the cavity resonance frequency is nearly invariant under different N_m , and the cavity Q/V first increases exponentially with increasing N_m owing to the mirror's strengthened optical confinement and effectively reduced scattering losses by the increased mirror periods, until it finally levels off when N_m is greater than 25. The high $Q/V \sim 3.26 \times 10^3$ of can be achieved. Compared to the cavity without mirror periods (i.e., $N_t = 20$, $N_m = 0$), the cavity Q/V is improved

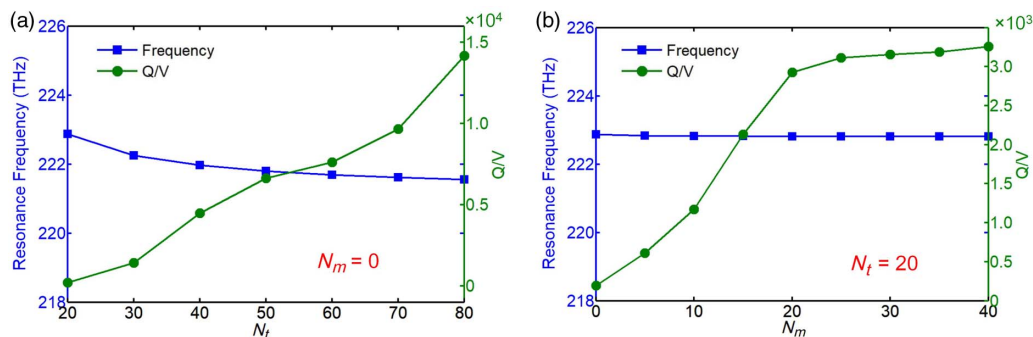


Fig. 6. (a) Influence of different hole grating number N_t (changed from $N_t = 20$ to $N_t = 80$) in the taper region of the proposed AM-PCNFC on cavity resonance frequency and Q/V , when $N_m = 0$. (b) Influence of different hole grating number N_m (changed from $N_m = 0$ to $N_m = 40$) in the mirror region of the proposed AM-PCNFC on cavity resonance frequency and Q/V , when $N_t = 20$. Other parameters are the same as $d_{\text{NF}} = 1.04$ μm , $a = 620$ nm, $r_{\text{center}} = 195$ nm, and $r_{\text{end}} = 240$ nm.

more than one order of magnitude. Figure 4(b) shows the top view of the major field distribution profile (E_y) in x - y plane of the proposed AM-PCNFC. It can be seen clearly that the AM is strongly localized in the air-holes region. This means the optical field can overlap sufficiently with the analytes within the air-holes region, allowing a strong light-matter interaction. Thus, the AM-PCNFC proposed in this work is potentially an ideal platform for high-performance RI sensing.

3. RI SENSITIVITY AND FOM OF PCNFC SENSOR

Next, in order to further discuss the RI sensing performances of the proposed DM-PCNFC sensor and AM-PCNFC sensor, we analyze and calculate the RI sensitivity and FOM of the proposed sensor device when it is immersed in an analyte with different RI values. Figure 7 shows the schematic diagram of the proposed PCNFC sensor, which is composed of dozens of air holes inscribed in the uniform waist region of a microfiber connected by two conical transition regions to conventional single-mode fibers (SMFs). In order to ensure the coupling of fundamental mode from the input of SMF to the tapered fiber with negligible loss, the tapered angle needs to be small enough to be approximately adiabatic. When the tapered transition region is adiabatic, the fundamental mode of the fiber shows no power exchange with the high-order mode and can be guided continuously through the tapered transition region [35,44]. The sensor device structure is symmetric with respect to its center. The diameter of the uniform waist region

is chosen to be $d_{\text{NF}} = 1.04 \mu\text{m}$. The periodicity of the air-hole gratings is $a = 620 \text{ nm}$.

Herein, to save the simulation time of the transmission calculation with the 3D-FDTD method, we use a high-transmission but low- Q -factor geometry. Figures 8(a) and 8(b) show the air-hole radii versus hole number along the length of the DM-PCNFC sensor and AM-PCNFC sensor, respectively. As seen, (1) for the DM-PCNFC sensor, the numbers of air-hole gratings in the taper region and mirror region of the DM-PCNFC sensor are chosen to be $N_t = 15$ and $N_m = 10$, respectively. The cavity taper region has a 30-hole defect consisting of a quadratic reduction in hole radius, decreased from $r_{\text{center}} = 230 \text{ nm}$ in the center to $r_{\text{end}} = 180 \text{ nm}$ on both ends. On either side of the defect is a mirror region, each consisting of 10 air-hole gratings with the same radius of $r_{\text{end}} = 180 \text{ nm}$. (2) For the AM-PCNFC sensor, the numbers of air-hole gratings in the taper region and mirror region of the AM-PCNFC sensor are chosen to be $N_t = 20$ and $N_m = 10$, respectively. The cavity taper region has a 40-hole defect consisting of a quadratic addition in hole radius, increased from $r_{\text{center}} = 195 \text{ nm}$ in the center to $r_{\text{end}} = 240 \text{ nm}$ on both ends. On either side of the defect is a mirror region, each consisting of 10 air-hole gratings with the same radius of $r_{\text{end}} = 240 \text{ nm}$.

By using the 3D-FDTD method, the total transmission spectrum for the fundamental mode of the proposed DM-PCNFC sensor and AM-PCNFC sensor are shown in Figs. 9(a) and 9(d), respectively, when the background RI = 1.0. As seen in Fig. 9(a), at the edges of the bandgap,

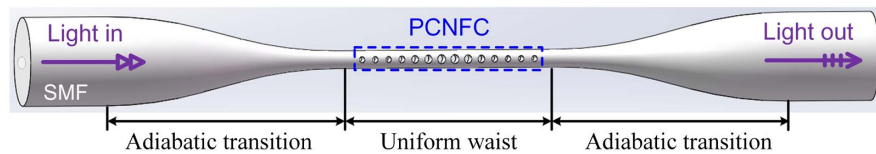


Fig. 7. Schematic diagram of the proposed PCNFC sensor. The sensor device structure is symmetric with respect to its center, which consists of air holes etched into the uniform waist part of a silica ($n_{\text{SiO}_2} = 1.45$) nanofiber waveguide with diameter $d_{\text{NF}} = 1.04 \mu\text{m}$. The periodicity of the air-hole gratings is $a = 620 \text{ nm}$.

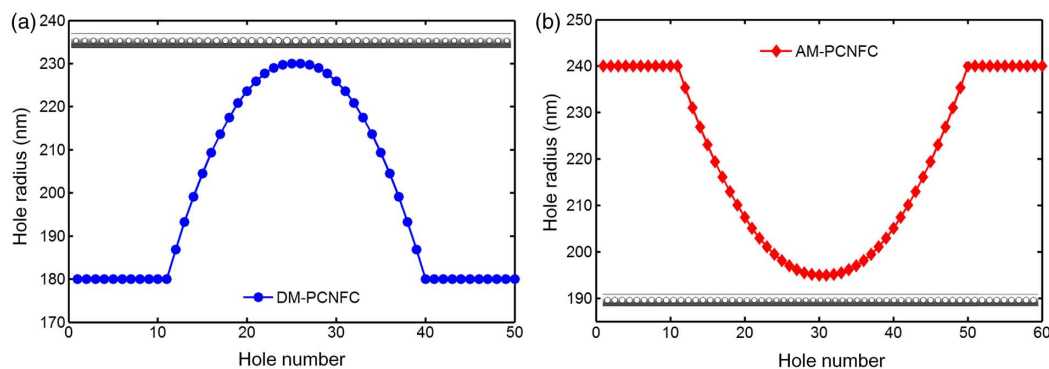


Fig. 8. (a) Air-hole radius versus hole number along the length of DM-PCNFC. The cavity taper region has a 30-hole defect consisting of a quadratic increasing in hole radius, increased from $r_{\text{end}} = 180 \text{ nm}$ on both ends to $r_{\text{center}} = 230 \text{ nm}$ in the center. On either side of the defect is a mirror region, each consisting of 10 air-hole gratings with the same radius of $r_{\text{end}} = 180 \text{ nm}$. (b) Air-hole radius versus hole number along the length of AM-PCNFC. The cavity taper region has a 40-hole defect consisting of a quadratic reduction in hole radius, decreased from $r_{\text{end}} = 240 \text{ nm}$ on both ends to $r_{\text{center}} = 195 \text{ nm}$ in the center. On either side of the defect is a mirror region, each consisting of 10 air-hole gratings with the same radius of $r_{\text{end}} = 240 \text{ nm}$.

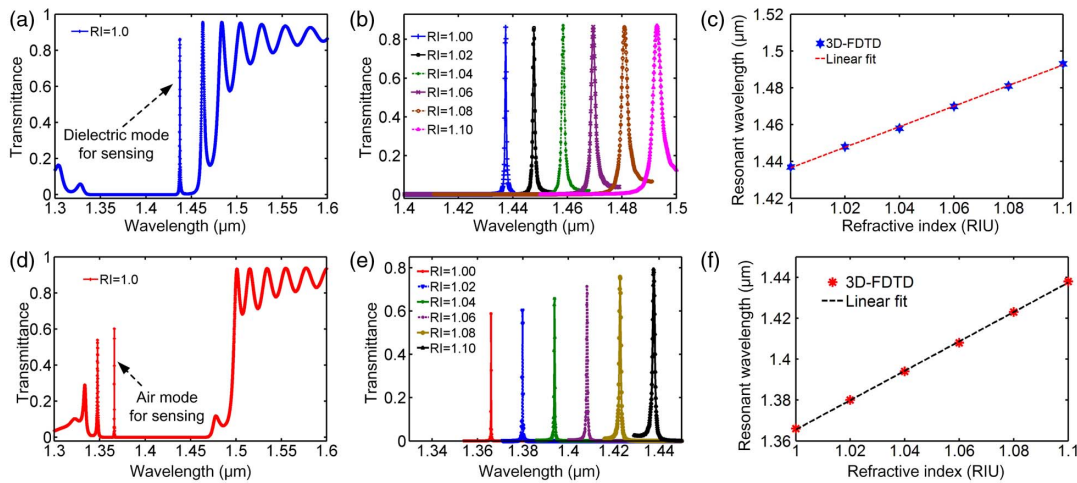


Fig. 9. Transmission spectrum for the fundamental mode of the optimized (a) DM-PCNFC sensor and (d) AM-PCNFC sensor structure from 3D-FDTD simulation. The background refractive index is set as RI = 1.0. Transmission spectra of the proposed (b) DM-PCNFC sensor and (e) AM-PCNFC sensor when the background refractive index changes from RI = 1.00 to RI = 1.10. Shift of the cavity resonant wavelength of (c) DM-PCNFC sensor and (f) AM-PCNFC sensor as a function of increased refractive index.

a DM with high Q -factor of 3.3×10^3 and over 86% transmission is obtained from the simulations. The resonant wavelength of DM used for RI sensing is 1437.33 nm. As seen in Fig. 9(b), an AM with high Q -factor of 9.8×10^3 and over 60% transmission is obtained from the simulations. The resonant wavelength of AM used for RI sensing is 1365.96 nm (219.6 THz), which agrees very well with the target resonant wavelength obtained at 218.3 THz from the band-diagram simulations, marked as red dots in the inset of Fig. 5(a). Next, to calculate the RI sensitivity (S) and FOM of the proposed DM-PCNFC sensor and AM-PCNFC sensor, respectively, Figs. 9(b) and 9(e) show the resonant wavelength shift when the background RI varies from RI = 1.00 to RI = 1.10 (Δ RI = 0.10). Figures 9(c) and 9(f) show the linear fit of the resonant wavelength shift (red shift) with increased RI. As seen, the resonant wavelength shifts ($\Delta\lambda$) of the DM-PCNFC sensor and AM-PCNFC sensor are 56.36 nm and 73.68 nm, respectively. Therefore, the RI sensitivities calculated by $S = \Delta\lambda/\Delta$ RI are $S_{DM} = 563.6$ nm/RIU and $S_{AM} = 736.8$ nm/RIU, resulting in the optimized FOMs as high as 4.31×10^6 and 1.13×10^5 , respectively. Therefore, the current design has a sufficiently high sensitivity and high Q for the purpose of most gas-sensing applications. In addition, with a FOM comparable to the sensors presented in the recent work [34], the proposed PCNFC sensor in this work has low-index contrast, which is reduced more than two times. Moreover, the structural simplicity of the proposed PCNFC sensor in this paper lends itself to easier fabrication. The experimental realization of the proposed PCNFC structure is generally technically achievable with modern nano-fabrication techniques. Several different approaches toward the fabrication of silica NF-based cavities have been reported, such as the femtosecond laser ablation technique [26] and focused ion beam (FIB) technique [33]. Thus, the proposed PCNFC sensor structure can be experimentally achieved in a freely suspended microfiber using the FIB milling technique, as demonstrated in previous works [33,45].

4. CONCLUSION

In summary, due to the radiation losses in the low-index-contrast systems, the design of ultrahigh Q -factor, small-mode-volume PC cavities has been elusive. Here, we reported two different designs of an ultra-compact PCNFC with ultrahigh Q -factor over 10^7 in silica NF possessing low-index contrast (ratio = 1.45). These cavities have much smaller mode volumes than the previously demonstrated NF-based FP cavities based on fiber Bragg gratings. In addition, for both DM and AM in the proposed PCNFC, we have shown that both the DM-PCNFC sensor and AM-PCNFC sensor can simultaneously possess high Q and high sensitivity. With 3D-FDTD simulations, the FOMs of the DM-PCNFC sensor and AM-PCNFC sensor as high as 4.31×10^6 and 1.13×10^5 have been obtained, respectively. Particularly, it is worth mentioning that the ability to realize high- Q/V nanophotonic cavities in a freely suspended optical NF makes these devices conveniently realize long-distance sensing applications without the need for complicated coupling systems, and free from the influence of substrates; thus, they are potentially ideal platforms for RI-based gas sensing and environmental monitoring.

Funding. National Natural Science Foundation of China (NSFC) (65101053); Fundamental Research Funds for the Central Universities (2018XKJC05); Fund of the State Key Laboratory of Information Photonics and Optical Communications (IPOC2017ZT05); Beijing University of Posts and Telecommunications.

REFERENCES

1. Y. Zhi, X. Yu, Q. Gong, L. Yang, and Y.-F. Xiao, "Single nanoparticle detection using optical microcavities," *Adv. Mater.* **29**, 1604920 (2017).
2. R. V. Nair and R. Vijaya, "Photonic crystal sensors: an overview," *Prog. Quantum Electron.* **34**, 89–134 (2010).

3. Y. Hang, Y. Zhao, and R. Lv, "A review for optical sensors based on photonic crystal cavities," *Sens. Actuators A* **233**, 374–389 (2015).
4. G. Shambat, S. Kothapalli, J. Provine, T. Sarmiento, J. Harris, S. Gambhir, and J. Vuckovic, "Single-cell photonic nanocavity probes," *Nano Lett.* **13**, 4999–5005 (2013).
5. Y. Chen, W. Fegadolli, W. Jones, A. Scherer, and M. Li, "Ultrasensitive gas-phase chemical sensing based on functionalized photonic crystal nanobeam cavities," *ACS Nano* **8**, 522–527 (2014).
6. D. Yang, H. Tian, Y. Ji, and Q. Quan, "Design of simultaneous high-Q and high-sensitivity photonic crystal refractive index sensors," *J. Opt. Soc. Am. B* **30**, 2027–2031 (2013).
7. D. Yang, S. Kita, F. Liang, C. Wang, H. Tian, Y. Ji, M. Loncar, and Q. Quan, "High sensitivity and high Q-factor nanoslotted parallel quadrabeam photonic crystal cavity for real-time and label-free sensing," *Appl. Phys. Lett.* **105**, 063118 (2014).
8. Q. Quan, D. Floyd, I. Burgess, P. Deotare, I. Frank, S. Y. Tang, R. Ilic, and M. Loncar, "Single particle detection in CMOS compatible photonic crystal nanobeam cavities," *Opt. Express* **21**, 32225–32233 (2013).
9. C. Wang, Q. Quan, S. Kita, Y. Li, and M. Loncar, "Single-nanoparticle detection with slot-mode photonic crystal cavities," *Appl. Phys. Lett.* **106**, 261105 (2015).
10. D. Yang, H. Tian, and Y. Ji, "High-Q and high-sensitivity width-modulated photonic crystal single nanobeam air-mode cavity for refractive index sensing," *Appl. Opt.* **54**, 1–5 (2015).
11. D. Yang, P. Zhang, H. Tian, Y. Ji, and Q. Quan, "Ultra-high-Q and low-mode-volume parabolic radius-modulated single photonic crystal slot nanobeam cavity for high-sensitivity refractive index sensing," *IEEE Photon. J.* **7**, 4501408 (2015).
12. F. Liang, Y. Guo, S. Hou, and Q. Quan, "Photonic-plasmonic hybrid single-molecule nanosensor measures the effect of fluorescent labels on DNA-protein dynamics," *Sci. Adv.* **3**, e1602991 (2017).
13. Y. Zhang, P. Liu, S. Zhang, W. Liu, J. Chen, and Y. Shi, "High sensitivity temperature sensor based on cascaded silicon photonic crystal nanobeam cavities," *Opt. Express* **24**, 23037–23043 (2016).
14. C. Feng, G.-Y. Feng, G.-R. Zhou, N.-J. Chen, and S.-H. Zhou, "Design of an ultracompact optical gas sensor based on a photonic crystal nanobeam cavity," *Laser Phys. Lett.* **9**, 875–878 (2012).
15. W. Liu, J. Yan, and Y. Shi, "High sensitivity visible light refractive index sensor based on high order mode Si₃N₄ photonic crystal nanobeam cavity," *Opt. Express* **25**, 31739–31745 (2017).
16. T. Li, D. Gao, D. Zhang, and E. Cassan, "High-Q and high-sensitivity one-dimensional photonic crystal slot nanobeam cavity sensors," *IEEE Photon. Technol. Lett.* **28**, 689–692 (2016).
17. P. Yu, H. Qiu, W. Wang, T. Hu, H. Yu, Z. Wang, F. Wu, X. Jiang, and J. Yang, "Analysis and design of refractive index biosensors based on single silicon nanobeam cavity," *IEEE Photon. J.* **8**, 3700110 (2016).
18. S. Kim, H. Kim, and Y. Lee, "Single nanobeam optical sensor with a high Q-factor and high sensitivity," *Opt. Lett.* **40**, 5351–5354 (2015).
19. S. Kim, H. Ko, C. Lee, M. Kim, K. Kim, Y.-H. Lee, K. Shin, and Y.-H. Cho, "Semiconductor photonic nanocavity on a paper substrate," *Adv. Mater.* **28**, 9765–9769 (2016).
20. D. Yang, F. Gao, Q.-T. Cao, C. Wang, Y. Ji, and Y.-F. Xiao, "Single nanoparticle trapping based on on-chip nanoslotted nanobeam cavities," *Photon. Res.* **6**, 99–108 (2018).
21. Y. Ooka, T. Tetsumoto, A. Fushimi, W. Yoshiki, and T. Tanabe, "CMOS compatible high-Q photonic crystal nanocavity fabricated with photolithography on silicon photonic platform," *Sci. Rep.* **5**, 11312 (2015).
22. T. Tetsumoto, Y. Ooka, and T. Takasumi, "High-Q coupled resonances on a PhC waveguide using a tapered nanofiber with high coupling efficiency," *Opt. Express* **23**, 16256–16263 (2015).
23. P. E. Barclay, K. Srinivasan, M. Borselli, and O. Painter, "Probing the dispersive and spatial properties of photonic crystal waveguides via highly efficient coupling from fiber tapers," *Appl. Phys. Lett.* **85**, 4–6 (2004).
24. L. Tong, R. R. Gattass, J. B. Ashcom, S. He, J. Lou, M. Shen, I. Maxwell, and E. Mazur, "Subwavelength-diameter silica wires for low-loss optical wave guiding," *Nature* **426**, 816–819 (2003).
25. J. E. Hoffman, S. Ravets, J. A. Grover, P. Solano, P. R. Kordell, J. D. Wong-Campos, L. A. Orozco, and S. L. Rolston, "Ultra-high transmission optical nanofibers," *AIP Adv.* **4**, 067124 (2014).
26. J. Keloth, K. P. Nayak, and K. Hakuta, "Fabrication of a centimeter-long cavity on a nanofiber for cavity quantum electrodynamics," *Opt. Lett.* **42**, 1003–1006 (2017).
27. K. P. Nayak, P. Zhang, and K. Hakuta, "Optical nanofiber based photonic crystal cavity," *Opt. Lett.* **39**, 232–235 (2014).
28. F. Xu, P. Horak, and G. Brambilla, "Optical microfiber coil resonator refractometric sensor," *Opt. Express* **15**, 7888–7893 (2007).
29. X. Fan, I. White, S. Shopova, H. Zhu, J. Suter, and Y. Sun, "Sensitive optical biosensors for unlabeled targets: a review," *Anal. Chim. Acta* **620**, 8–26 (2008).
30. G. Y. Chen, M. Ding, T. P. Newson, and G. Brambilla, "A review of microfiber and nanofiber based optical sensors," *Open Opt. J.* **7**, 32–57 (2013).
31. J. Lou, Y. Wang, and L. Tong, "Microfiber optical sensors: a review," *Sensors* **14**, 5823–5844 (2014).
32. X.-C. Yu, B.-B. Li, P. Wang, L. Tong, X.-F. Jiang, Y. Li, Q. Gong, and Y.-F. Xiao, "Single nanoparticle detection and sizing using a nanofiber pair in an aqueous environment," *Adv. Mater.* **26**, 7462–7467 (2014).
33. Y. Yu, T. Xiao, H. Guo, and Z.-Y. Li, "Sensing of microparticles based on a broadband ultrasmall microcavity in a freely suspended microfiber," *Photon. Res.* **5**, 143–150 (2017).
34. C. Deng, M. Li, J. Peng, W. Liu, and J. Zhong, "Simultaneously high-Q and high-sensitivity slotted photonic crystal nanofiber cavity for complex refractive index sensing," *J. Opt. Soc. Am. B* **34**, 1624–1631 (2017).
35. T. Tu, F. Pang, S. Zhu, J. Cheng, H. Liu, J. Wen, and T. Wang, "Excitation of Bloch surface wave on tapered fiber coated with one-dimensional photonic crystal for refractive index sensing," *Opt. Express* **25**, 9019–9027 (2017).
36. X.-C. Yu, Y. Zhi, S.-J. Tang, B.-B. Li, Q. Gong, C.-W. Qiu, and Y.-F. Xiao, "Optically sizing single atmospheric particulates with a 10-nm resolution using a strong evanescent field," *Light Sci. Appl.* **7**, 18003 (2018).
37. L. Tong, "Micro/nanofiber optical sensors: challenges and prospects," *Sensors* **18**, 903 (2018).
38. A. Muller, E. B. Flagg, J. R. Lawall, and G. S. Solomon, "Ultra-high-finesse, low-mode-volume Fabry-Perot microcavity," *Opt. Lett.* **35**, 2293–2295 (2010).
39. J. Ma, J. Ju, L. Jin, W. Jin, and D. Wang, "Fiber-tip micro-cavity for temperature and transverse load sensing," *Opt. Express* **19**, 12418–12426 (2011).
40. Q. Zhang, L. Hu, Y. Qi, G. Liu, N. Ianno, and M. Han, "Fiber-optic refractometer based on a phase-shifted fiber Bragg grating on a side-hole fiber," *Opt. Express* **23**, 16750–16759 (2015).
41. K. Zhou, Z. Yan, L. Zhang, and I. Bennion, "Refractometer based on fiber Bragg grating Fabry-Perot cavity embedded with a narrow micro-channel," *Opt. Express* **19**, 11769–11779 (2011).
42. Q. Quan and M. Loncar, "Deterministic design of wavelength scale, ultra-high Q photonic crystal nanobeam cavities," *Opt. Express* **19**, 18529–18542 (2011).
43. <https://www.lumerical.com/tcad-products/fdtd/>.
44. J. D. Love, W. M. Henry, W. J. Stewart, R. J. Black, S. Lacroix, and F. Gonthier, "Tapered single-mode fibers and devices. I. Adiabaticity criteria," *IEEE Proc. J. Optoelectron.* **138**, 343–354 (1991).
45. K. P. Nayak, F. Le Kien, Y. Kawai, K. Hakuta, K. Nakajima, H. T. Miyazaki, and Y. Sugimoto, "Cavity formation on an optical nanofiber using focused ion beam milling technique," *Opt. Express* **19**, 14040–14050 (2011).